Research Square

Preprints are preliminary reports that have not undergone peer review.
They should not be considered conclusive, used to inform clinical practice,
or referenced by the media as validated information.

Separating Motion Artifacts from Biomarker Signals in Flexible MoS2 FET Cortisol Sensors: A Coupled Multiphysics Model and Finite-Element Analysis of Strain-Binding Cross-Talk and Mitigation Strategies

Ayomide Adeyemi

ayowilfred1995@gmail.com

Kwara State University

Victor Ogunyemi

Olabisi Onabanjo University

Research Article

Keywords: Wearable biosensor MoS2 field-effect transistor Motion artifact Finite-element analysis Multiphysics simulation Cortisol

Posted Date: November 4th, 2026

DOI: https://doi.org/10.21203/rs.3.rs-11606589/v1

License: This work is licensed under a Creative Commons Attribution 4.0 International License.
Read Full License

Additional Declarations: The authors declare no competing interests.

Separating Motion Artifacts from Biomarker Signals in Flexible MoS_2 FET Cortisol Sensors: A Coupled Multiphysics Model and Finite-Element Analysis of Strain-Binding Cross-Talk and Mitigation Strategies

Ayomide Adeyemi[1,*] · **Victor Ogunyemi**[2]

[1] Department of Electrical and Electronics Engineering, Kwara State University, Malete, Nigeria

[2] Department of Electrical and Electronics Engineering, Olabisi Onabanjo University, Ago-Iwoye, Nigeria

[*] Corresponding author: Ayomide Adeyemi, ayowilfred1995@gmail.com

Victor Ogunyemi: ogunyemivictor738@gmail.com

Abstract

Flexible molybdenum disulfide (MoS_2) field-effect transistor (FET) biosensors can monitor cortisol in sweat, but their atomically thin channel is strongly piezoresistive, so body movement produces current changes that resemble hormone signals. We present a six-stage multiphysics model that links wrist and elbow flexion and walking to a strain-equivalent false cortisol concentration. Channel strain is computed by plane-strain finite-element analysis in the open-source solver Elmer, verified against laminate beam theory, and drives compact models of piezoresistance, Schottky-barrier lowering, strain-binding cross-talk, aptamer kinetics and Debye screening. For a 25 μm polyimide patch the model predicts wrist flexion produces a current artifact of 44% of the full-scale cortisol response and walking 5 to 11 ng/mL of false cortisol, with about 70% of the artifact arising at the Schottky contacts. Low-pass filtering leaves the non-zero mean of unipolar flexion (22% of full scale). Twin-sensor subtraction is limited by gauge mismatch and by a cross-talk floor proportional to aptamer occupancy, 1.0 to 2.8% of full scale across the physiological range at the wrist. With a 2.5 μm substrate and matched twin channels the residual falls to 0.9 to 1.3 ng/mL, not consistently below a 1 ng/mL target at the wrist for the assumed affinity. A rigid island under the channel retains 18 to 109% of the baseline strain under end-moment loading and about 300% when the skin imposes the curvature, so it fails to isolate the channel in bending. The predicted magnitudes scale with the assumed threshold shift; design guidelines by body location are given.

Keywords: Wearable biosensor · MoS_2 field-effect transistor · Motion artifact · Finite-element analysis · Multiphysics simulation · Cortisol

1. Introduction

Cortisol is the principal human stress hormone, and its concentration in sweat is a candidate marker for continuous, non-invasive monitoring of stress, sleep disturbance and endocrine disorders. Wearable cortisol sensors based on aptamer-functionalised field-

effect transistors (FETs) have progressed from bench devices to a smartwatch that resolves picomolar changes in artificial sweat [1, 2, 3]. Two-dimensional semiconductors, and molybdenum disulfide (MoS_2) in particular, are strong candidates for the transistor channel. Their sub-nanometre thickness exposes every carrier to the surface where binding occurs, giving femtomolar detection limits in laboratory buffer [4, 5], and atomically thin films tolerate the bending radii of a skin-mounted patch [6, 7].

The same thinness is the source of a serious measurement problem. Strain shifts the MoS_2 bandgap, modulates carrier mobility and lowers the metal-MoS_2 Schottky barrier, so a flexible MoS_2 FET is also an excellent strain gauge. Gate-dependent gauge factors up to 200 have been measured in monolayer devices on flexible substrates [8]; a strain of only a few tenths of a percent applied electrically changed drain current by more than two orders of magnitude [9]; and tensile strain lowers the contact barrier by roughly 55 meV per percent [10]. Strain does not simply add an offset. It also changes the chemical sensitivity of the device itself, by 29 percent over a strain range of only 0.34 percent in flexible MoS_2 ion sensors [11]. The authors of the closest experimental study to ours found that, without mechanical protection, they could not attribute a resistance change to cortisol rather than to bending [12]. The authors of prebent MoS_2 biosensors had earlier identified strain-induced false readings as a barrier to wearable two-dimensional biosensors [13].

Existing work addresses one link of this chain at a time. Structural studies compute how much strain reaches a sensing layer, for example a thousandfold reduction for prebent channels [13], or a sensing-region strain equal to 4.2 percent of the stretched-region strain in decoupled iontronic sensors [14], but stop at the mechanics. Such isolation ratios are also often quoted for one loading mode and reused for another; whether a ratio obtained in stretching holds in bending, the dominant deformation of a skin patch over a joint, has not been checked. Device studies measure the electrical response to a static bend and report that the sensor still works [5, 12, 15]. They do not translate the residual change into an equivalent false concentration, do not consider the sweat electrolyte in which the real signal is strongly attenuated by Debye screening [3, 16], and do not consider repeated dynamic motion, the normal condition of a worn device. Signal-level compensation using a scrambled-aptamer reference channel has been demonstrated on In_2O_3 aptamer FETs [1] but has never been evaluated against motion artifacts specifically. The motion-artifact literature for electrophysiological electrodes is mature and well classified [17], but its mechanisms (skin-electrode impedance changes) differ from those of a chemiresistive or FET biosensor, in which motion changes the semiconductor itself.

To our knowledge, these links have not been combined in one quantitative model. Relative to the closest studies, the present work differs as follows. Aleksandrova et al. [12] measured MoS_2 cortisol chemiresistors after cyclic bending in a non-aqueous medium; here a liquid-gated FET is modelled during motion in a sweat-like electrolyte. Ryu et al. [13] and Shen et al. [14] quantified strain isolation for one structure and one loading mode; here seven structures are compared under the same bending motions and the same electrical chain, and the loading mode itself is varied. Li et al. [11] measured the strain dependence of sensitivity that is used here as the cross-talk coefficient, and Wang et al. [1]

demonstrated a reference channel without motion; here the two are combined to quantify what reference subtraction can and cannot remove. The contribution is therefore the integration of known effects into one model and the comparison of mitigations under identical conditions, not a new physical mechanism. The specific contributions are:

1. A six-stage, fully parameterised model with documented simulation procedures linking wrist flexion, elbow flexion and walking to the current of a liquid-gated MoS_2 FET cortisol sensor operating in sweat, with the mechanics solved by finite elements in the open-source Elmer FEM.
2. A physiological-range-referenced error metric, the strain-equivalent false cortisol concentration, compared against the reported sweat range of 8.16 to 141.7 ng/mL [12].
3. An explicit decomposition of the artifact into channel piezoresistance, Schottky-contact modulation and strain-sensitivity cross-talk.
4. A time-domain analysis showing when timescale filtering can and cannot separate motion from binding kinetics, including the failure mode caused by the non-zero mean of unipolar flexion.
5. A like-for-like ranking of seven structural strategies, gate-bias selection and twin-sensor subtraction, including an FE demonstration, under two loading assumptions, that a rigid island under the channel protects far less in bending than in stretching, leading to design guidelines by body location.

The study is simulation-only, and all results are model predictions intended to guide fabrication rather than replace it. Each parameter is either taken from a cited measurement or labelled as an assumption (Section 2.7), and the influence of the most uncertain ones is quantified in Appendix D. The physiological range is used as a scale for the errors, not as a clinically validated decision threshold.

2. Simulation Framework

The framework (Fig. 1) is a chain of six stages. Stage 2, the mechanics, is solved by finite elements in Elmer FEM 9.0 (ElmerSolver 26.2) [28], an open-source multiphysics code developed by CSC – IT Center for Science (Finland), and the results are viewed in ParaView 5.11 [29]. The electrical, electrochemical and signal-processing stages (3 to 6) are compact models implemented in Python (NumPy and SciPy) and driven by the FE channel strain. Each stage uses published coefficients, so the sensitivity of the final error to any assumption can be examined by changing one parameter. A compact chain was preferred to an industrial device simulator for Stages 3 to 6 because it can be run thousands of times inside a time-domain loop; the parameter-extraction procedure of [18] provides the route to reproducing the electrical stages in such a simulator if finer device detail is later required.

Fig. 2(a) shows the modelled device: a liquid-gated MoS_2 FET on a flexible polyimide substrate with gold source and drain electrodes; a 5 nm atomic-layer-deposited Al_2O_3 passivation and linker layer, as used in the MoS_2 cytokine and immunoglobulin sensors of

[4, 5]; an anti-cortisol DNA aptamer as the recognition element [1]; and sweat as the gate electrolyte, with a reference electrode setting the gate potential, the most common configuration for FET biosensing [7].

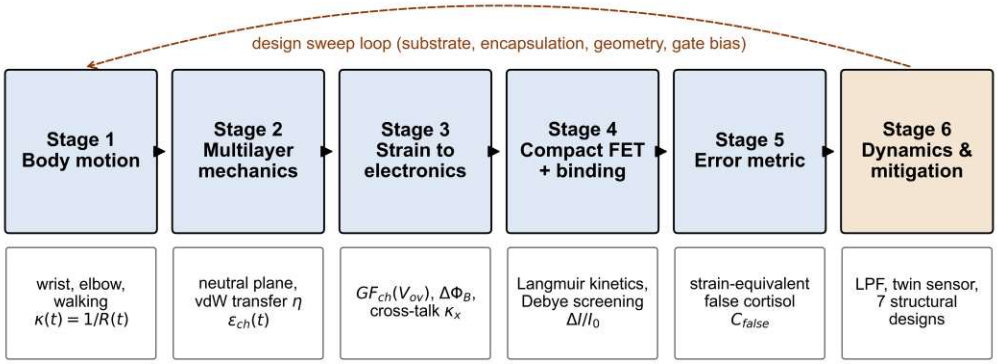


Fig. 1 *Six-stage simulation chain from body motion to false cortisol reading. Stages 1 to 5 form the forward model; Stage 6 applies signal-level compensation and drives the design sweep. Stage 2 is solved in Elmer FEM.*

2.1 Stage 1: Body Motion to Patch Curvature

A patch bonded to skin follows the local surface curvature, so body motion is represented as a time-varying curvature κ(t) = 1/R(t) of the patch. Three motions relevant to a forearm- or wrist-mounted device are modelled (parameters in Section 2.7). Wrist flexion and elbow flexion are unipolar: the patch goes from flat to a minimum bending radius and back,

$$\kappa(t) = \frac{1}{2R_{\min}}[1 - \cos(2\pi f t)] \qquad (1)$$

with R_{min} = 25 mm for the dorsal wrist and 40 mm for the elbow, and a repetition frequency f = 0.5 Hz typical of gesturing and lifting. Skin-strain measurements at the wrist joint reach several tens of percent during flexion [19], far above the failure strain of any device stack; a patch that does not slip must therefore be placed on the dorsal wrist rather than across the joint crease, where it bends around the wrist bones with the radii adopted here. Walking produces arm swing and forearm muscle activity that perturb the static curvature of the forearm. This is modelled as a bipolar oscillation $\kappa(t) = \kappa_0 + \Delta\kappa \sin(2\pi f t)$ with $1/\Delta\kappa$ = 300 mm at the mean pacing frequency of 1.8 Hz [20]. The static curvature κ_0 is present when the sensor is calibrated on the body and therefore cancels; only changes in curvature generate an artifact. A fourth case, sustained wrist flexion held at R = 30 mm (for example while holding a phone), tests the failure mode of timescale filtering. These waveforms are idealised and are not measured patch-level traces; they do not represent all users or placements. Skin slip, adhesive compliance and placement change the curvature actually transferred to the patch, which is equivalent to changing R_{min} or η; Appendix D gives the results over R_{min} = 20 to 40 mm and η = 0.5 to 1.0.

2.2 Stage 2: Curvature to Channel Strain (Finite-Element Model)

In a bent laminate the strain in each layer is set by its distance from the neutral plane, whose position z_n is, in one-dimensional beam theory, the modulus-weighted centroid of the stack [21]:

$$z_n = \frac{\sum_i E_i\, t_i \bar{z}_i}{\sum_i E_i\, t_i} \qquad (2)$$

where E_i, t_i and $\bar{z}_i$ are the Young's modulus, thickness and mid-plane height of layer i measured from the bottom of the substrate. Because the MoS_2 channel is bonded to the substrate by van der Waals forces only, it receives a fraction η of the strain of a perfectly bonded film at its position; polymer encapsulation roughly doubles this transfer by suppressing interfacial slip [22]. The channel strain is therefore

$$\varepsilon_{ch} = \eta\,(z_{ch} - z_n)\,\kappa \qquad (3)$$

with η = 0.5 for a bare channel, 0.8 under a thin conformal Al_2O_3 cap and 1.0 under a polymer cap. Equation (2) ignores the Poisson mismatch between layers and cannot represent designs whose stiffness varies along the patch, such as a rigid island. The quantity that matters downstream, the channel strain per unit curvature ε_{ch}/κ, is therefore computed by finite elements for every design.

Model. Each stack is modelled in Elmer as a two-dimensional, plane-strain, linear-elastic solid (StressSolver), which is appropriate for a patch whose width is large compared with its thickness. Strains are below 0.05 percent, so the analysis is geometrically linear and ε_{ch}/κ does not depend on the bend magnitude. Every layer, including the 0.65 nm MoS_2 film, is meshed as a solid with quadratic (eight-node) quadrilateral elements, one element through each nanometre film. Plane strain requires Poisson ratios, which the beam model of (2) does not: ν = 0.34 for polyimide, 0.44 for Au, 0.27 for MoS_2, 0.24 for Al_2O_3, 0.38 for PET, 0.35 for PMMA, 0.49 for PDMS and 0.22 for the island material (standard literature values).

Loading. Pure bending is applied as a force-free linear traction $\sigma_{xx} = s(y - y_{mid})$ on the end face. It carries a bending moment with zero net axial force, so the neutral plane is an outcome of the solution rather than an input. The load is scaled to give the wrist curvature (R = 25 mm) for display only; the reported ε_{ch}/κ is independent of it.

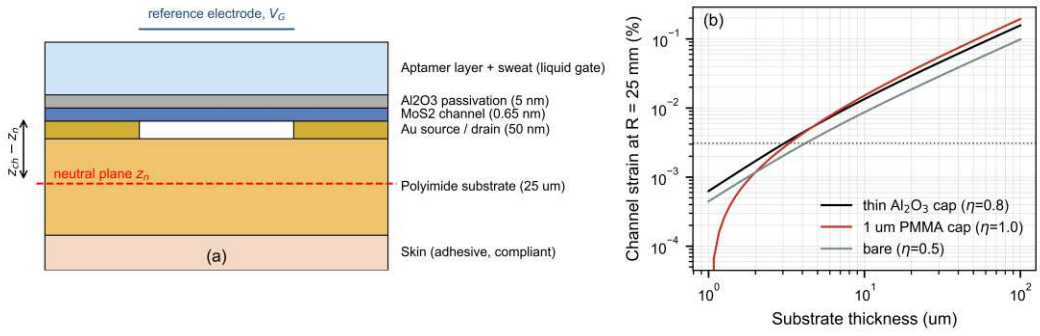
Domain. Elements 100 μm long and 0.65 nm thick are numerically ill-conditioned: on the full 10 mm strip, the computed curvature varied by more than 100 percent along a strip that must bend uniformly. Trials showed that element aspect ratios must stay below about 100. Because pure bending is uniform along the strip, any slice carries the same state, so every uniform design is modelled as a 200 μm half-slice with a mirror-symmetry plane at the channel centre, meshed with elements about 59 nm long (aspect ratio 90 in the MoS_2). Strain at the channel centre and 50 μm away agree to 4×10^{-8} (relative), confirming uniform bending. The channel strain is read at the MoS_2 mid-plane at the channel centre and multiplied by η.

Mesh convergence and verification. The linear systems are solved directly (UMFPACK), so no iterative tolerance enters the results. The convergence metric is the relative change of ε_{ch}/κ, the only mechanical output passed to the electrical chain, against the finest mesh. Table 1 gives the study for the baseline stack, with refinement along the strip and through the substrate together: ε_{ch}/κ changes by less than 10^{-4} percent between all four levels, as expected, because the strain field of pure bending is linear through each layer and is represented exactly by quadratic elements; the neutral-plane position z_n is equally stable. The same four levels applied to the 2.5 μm PET stack change ε_{ch}/κ by at most 0.007 percent, and halving or doubling the mesh of the rigid-island strip changes its channel strain by at most 0.025 percent (Appendix E). Level 3 is used throughout. To verify the setup, all Poisson ratios were set to zero, which reduces plane strain to the beam theory of (2): Elmer then gives z_n = 13.4326 μm (beam theory: 13.4326 μm) and ε_{ch}/κ = 11.6105 μm at η = 1 (beam theory: 11.6177 μm, a 0.06 percent difference due to reading nodal strain inside the single-element MoS_2 layer).

Table 1 Mesh convergence of the baseline stack (Elmer, plane strain).

Level	Elements	Degrees of freedom	Element length (nm)	PI element rows	ε_{ch}/κ, bonded (μm)	z_n (μm)
1	11,900	78,230	118	4	11.55611	13.48701
2	21,600	139,238	83	6	11.55611	13.48701
3 (used)	37,400	238,046	59	8	11.55611	13.48701
4	72,000	451,262	42	12	11.55612	13.48701

Baseline result. For the baseline stack (25 μm polyimide, 50 nm Au, 0.65 nm MoS_2, 5 nm Al_2O_3) Elmer gives z_n = 13.487 μm, so the channel sits 11.56 μm above the neutral plane and ε_{ch}/κ = 9.245 μm with η = 0.8. Plane strain stiffens each layer by $1/(1-\nu^2)$; because Au has a higher Poisson ratio than polyimide, the neutral plane moves up by 0.4 percent and the channel strain is 0.53 percent lower than beam theory predicts. Fig. 2(b) shows the beam-theory channel strain versus substrate thickness for three cap conditions, and Fig. 2(c) the Elmer strain field of the baseline stack at R = 25 mm.



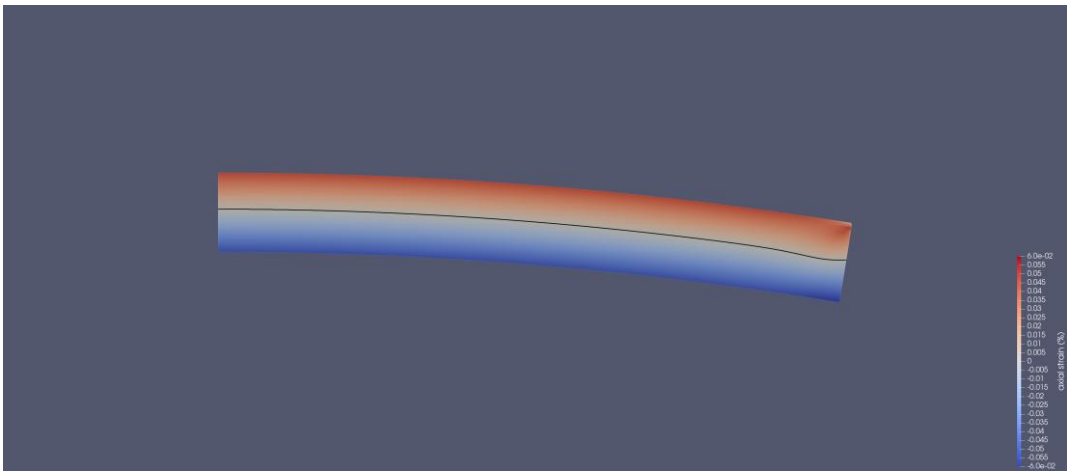


Fig. 2 *(a) Cross-section of the modelled liquid-gated MoS_2 FET cortisol sensor (not to scale) with the neutral plane of the baseline stack. (b) Channel strain at a bending radius of 25 mm versus substrate thickness for three cap conditions from (2) and (3); the dotted line marks the walking-induced strain of the baseline device. (c) Axial strain in the baseline stack at R = 25 mm computed by Elmer (bend exaggerated ×20); positive values are tension and negative values compression (colour scale), and the solid line is the computed neutral plane.*

Design variants. A thinner substrate (12.5 µm PI), an ultrathin substrate (2.5 µm PET) and polymer encapsulation (1 µm PMMA over the Al_2O_3, η = 1) are modelled as uniform stacks. A buried channel near the neutral plane with an exposed extended gate, in the spirit of the remote-gate architecture of [3], is modelled by adding 23 µm of polyimide above the films; the 2 µm asymmetry places the channel 0.98 µm from the computed neutral plane, so the placement offset is an outcome of the geometry. A prebent channel is an out-of-plane prebuckled structure that a two-dimensional model cannot represent; its published strain ratio of 1×10^{-3} [13] is applied to the Elmer baseline.

Rigid island. The island (3 mm × 20 µm, E = 70 GPa) is embedded flush in a PDMS carrier (E = 2 MPa, 100 µm thick unless stated) under the 25 µm polyimide device film, below the channel. Because the island is shorter than the 10 mm patch, the state varies along the strip, and a 5 mm half-strip with symmetry at the centre is modelled. The nanometre films are omitted in this model: their bending stiffness is 0.3 percent of the island region's, and the channel strain is obtained from the polyimide surface strain plus 50 nm times the local curvature, which is exact for bonded thin films in bending. Two loading assumptions bound how a skin-mounted patch is bent. Under end-moment loading, the moment is applied through the polyimide end face, the patch bends freely, and the curvature that defines ε_{ch}/κ is the strip-average curvature (total rotation divided by length); this corresponds to a patch that is loosely coupled to the skin and bends as a whole. Under skin-imposed curvature, the PDMS underside is forced onto a circular arc of the wrist radius, either bonded (no stretching of the underside) or free to slide along it; this corresponds to a patch firmly attached to skin that dictates its shape. Equilibrium was checked for the moment-loaded case: the bending moment is constant to within the solver tolerance along the whole strip.

Boundary conditions are listed in Appendix E. The carrier thickness was not specified by the source design, so it is swept from 50 to 500 μm (Section 3.6).

2.3 Stage 3: Channel Strain to Electrical Parameters

Three strain effects are included. First, the channel is piezoresistive with a gate-dependent gauge factor. Reference [8] reports that the gauge factor of monolayer MoS_2 FETs is tunable by more than an order of magnitude with gate voltage and reaches 200 near threshold, and that current nearly doubles at 0.7 percent tensile strain. Both observations are captured by

$$GF_{ch}(V_{ov}) = GF_{\min} + (GF_{\max} - GF_{\min}) \exp\left(-\frac{V_{ov} - V_0}{V_g}\right) \qquad (4)$$

with $V_{ov} = V_G - V_T$ the gate overdrive, $GF_{min} = 15$, $GF_{max} = 200$, $V_0 = 0.05$ V and $V_g = 0.12$ V. Second, tensile strain lowers the Schottky barrier at the Au contacts by $\Delta\Phi_B = \beta\varepsilon_{ch}$ with $\beta = -5.5$ eV per unit strain (−55 meV per percent) [10], and the thermionic contact resistance scales as $\exp(\Delta\Phi_B/kT)$. Treating the device as a channel resistance in series with two contacts that carry a fraction r_c of the zero-strain resistance,

$$\frac{R(\varepsilon)}{R_0} = (1 - r_c)\, e^{-GF_{ch}\,\varepsilon} + r_c\, e^{\beta\varepsilon/kT}, \qquad \left.\frac{\Delta I}{I_0}\right|_{strain} = \frac{R_0}{R(\varepsilon)} - 1 \qquad (5)$$

where the exponential form of the channel term reduces to $1 - GF_{ch}\varepsilon$ at small strain and remains physical at large strain. For small strain the total gauge factor is

$$GF_{tot} = (1 - r_c)\, GF_{ch} + r_c \left(-\frac{\beta}{kT}\right) \qquad (6)$$

in which the contact term $-\beta/kT$ evaluates to 213 at 300 K. With $r_c = 0.3$, a value consistent with the Schottky-limited transport of exfoliated-flake MoS_2 devices with Cr/Au contacts [4, 10], and $V_{ov} = 0.3$ V, (6) gives $GF_{ch} = 38$ and $GF_{tot} = 90$, so the contacts supply about 70 percent (64 of 90) of the strain response. Third, strain changes the chemical sensitivity of the device. The 29 percent change over 0.34 percent strain measured in [11] is represented by a multiplicative cross-talk coefficient $\kappa_x = 85$ per unit strain applied to the biomarker response, (9) below. This term is what makes the problem one of strain-binding cross-talk rather than of simple additive noise.

2.4 Stage 4: Binding Kinetics and Compact FET Model

Cortisol binding to the immobilised aptamer follows Langmuir kinetics for the fractional occupancy θ,

$$\frac{d\theta}{dt} = k_{on}\, C\, (1 - \theta) - k_{off}\, \theta, \qquad \theta_{eq} = \frac{C}{C + K_D} \qquad (7)$$

with C the sweat cortisol concentration. Reported dissociation constants for cortisol aptamers span nanomolar to micromolar values [1, 23]. For the aptamer of [1] the constant is 500 nM in solution but about 30 pM on the FET surface; with 30 pM the

occupancy would exceed 0.998 over the whole physiological range (22 to 391 nM), leaving no concentration resolution, and with 500 nM it would span only 0.04 to 0.44. Both bounds are evaluated in Appendix D. The model uses an intermediate K_D = 50 nM (18.1 ng/mL), which places the steepest part of the binding isotherm inside the physiological range, and $k_{off} = 2\times10^{-3}$ s^{-1}, so that $k_{on} = k_{off}/K_D = 4.0\times10^{4}$ M^{-1} s^{-1} and the binding time constant $1/(k_{on}C + k_{off})$ is 77 s at 100 ng/mL, consistent with the one- to five-minute response times measured for MoS_2 cortisol sensors [12]. Following the aptamer-FET mechanism established in [16], binding causes a conformational change that redistributes the charged aptamer backbone within the electrical double layer. The unscreened threshold-voltage shift $\Delta V_{T,vac}$ produced by full cortisol coverage of a MoS_2 channel has been predicted by combined density-functional and device simulation to lie between 27 and 780 mV [24]; a conservative 100 mV is used. In sweat the shift is attenuated by Debye screening,

$$\Delta V_T = \Delta V_{T,vac} \exp\left(-\frac{d}{\lambda_D}\right), \qquad \lambda_D\,[\mathrm{nm}] = \frac{0.304}{\sqrt{I}} \qquad (8)$$

where I is the ionic strength in mol/L and d = 2 nm is the effective distance of the redistributed charge from the channel surface [25]. Sweat has an ionic strength of tens of millimoles per litre, dominated by sodium and chloride [26]; at I = 50 mM, λ_D = 1.36 nm and the full-coverage shift is reduced to 23.0 mV. In the linear regime of a liquid-gated FET, $I_D = \mu C_{dl}(W/L)(V_{ov} + \Delta V_T)V_D$, so the normalised biomarker response and its strain cross-talk are

$$R_{bio} = \frac{\Delta V_T\,\theta}{V_{ov}}\,(1 + \kappa_x\,\varepsilon_{ch}) \qquad (9)$$

At V_{ov} = 0.3 V the full-scale (saturated aptamer) response is 7.66 percent of I_0, and the physiological range from 8.16 to 141.7 ng/mL spans responses from 2.38 to 6.79 percent (Fig. 4(b)). This small span, a direct consequence of screening in sweat [3], is the reason strain artifacts of a few percent are so damaging.

2.5 Stage 5: Strain-Equivalent False Concentration

The measured response is the sum of the biomarker term and the strain term,

$$R_{meas} = R_{bio}(\theta, \varepsilon_{ch}) + \left.\frac{\Delta I}{I_0}\right|_{strain} \qquad (10)$$

A user of the sensor reads R_{meas} back through the strain-free calibration curve. Inverting (9) and the Langmuir isotherm gives the apparent concentration,

$$\theta_{app} = \frac{R_{meas}\,V_{ov}}{\Delta V_T}, \qquad C_{app} = K_D\,\frac{\theta_{app}}{1 - \theta_{app}} \qquad (11)$$

and the error metric is $C_{false} = C_{app} - C_0$, where C_0 is the true concentration at the operating point. If $\theta_{app} \geq 1$ the reading exceeds full scale and is reported as saturated. Because the isotherm is non-linear, the same current artifact produces a larger false concentration at higher true concentrations, so results are reported both as a percentage of the full-scale

response, which is independent of the operating point, and as C_{false} at stated operating points. Linearised errors, where quoted, divide the current artifact by the calibration slope dR/dC at C_0 and are given separately from this non-linear inversion; Appendix B works through both for walking and wrist flexion.

2.6 Stage 6: Dynamic Analysis and Signal-Level Compensation

The time-domain scenario lasts 1800 s at a 20 Hz sampling rate. True sweat cortisol steps from 30 to 100 ng/mL at t = 300 s, representing an acute stress response, and the aptamer occupancy follows (7). Motion is scheduled in 300 s blocks: rest, walking, wrist flexion cycles, sustained wrist flexion, elbow flexion cycles and rest. The FE value of ε_{ch}/κ for each design converts the scheduled curvature into channel strain. Two compensation methods are compared. Timescale filtering exploits the separation between motion (0.5 to 2 Hz) and binding (time constants of minutes) using a second-order Butterworth low-pass filter with cut-off f_c = 10 mHz, which attenuates a 0.5 Hz component by 68 dB in a single pass (136 dB in the forward-backward form). In the main results it is applied offline to the whole 1800 s record as a zero-phase forward-backward filter (SciPy sosfiltfilt, odd-symmetric padding of 9 samples at each end). This retrospective processing has no delay but is non-causal and cannot run unchanged on a wearable; Appendix C repeats the analysis with the causal (real-time) form of the same filter. Twin-sensor subtraction uses a co-located reference FET carrying a non-binding scrambled aptamer, as in [1], which experiences the same strain but no cortisol. Both outputs are normalised to their own zero-strain current, the reference has the same contact fraction and cross-talk coefficient, and its strain response differs from that of the sensing channel only by a gain mismatch $\delta = (G_{ref} - G_{sense})/G_{sense}$. Subtracting the two (Appendix A) gives

$$R_{twin} = R_{meas} - (1+\delta)\left.\frac{\Delta I}{I_0}\right|_{strain} = \frac{\Delta V_T\,\theta}{V_{ov}}(1+\kappa_x\varepsilon_{ch}) - \delta\left.\frac{\Delta I}{I_0}\right|_{strain} \qquad (12)$$

The additive strain term cancels; two residuals remain, both fractions of I_0: the cross-talk term $(\Delta V_T\theta/V_{ov})\kappa_x\varepsilon_{ch}$, which survives because the reference has no biomarker signal for strain to modulate, and the mismatch term $-\delta\,\Delta I/I_0$. For $\delta > 0$ the two partly cancel; for $\delta < 0$ they add. Because the sign of δ is not controlled in fabrication, results are given for matched devices ($\delta = 0$) and for $\delta = \pm 5$ percent, representative of neighbouring devices on one substrate. Errors are reported as the root-mean-square and maximum deviation from the ideal motion-free reading within each motion block; Appendix C also gives motion-only errors, which compare against the same processing applied without motion and so exclude the filter's response to the cortisol step.

2.7 Parameters and Model Checks

Table 2 lists every parameter with its source or marks it as an assumption. Table 3 reports consistency checks against published quantities, together with the FE verification. The series form of (5), in which the channel and contact resistances add, follows [10], where the strain responses of the channel and of the Schottky barriers were extracted separately; only the barrier coefficient β is taken from that work, and the channel gauge factor comes

from [8]. The Debye length at 100 mM reproduces the approximately 1 nm screening distance discussed in [16, 25]. The channel term of (5) reproduces the near-doubling of current at 0.7 percent strain reported in [8] at V_{ov} = 0.145 V, where GF_{ch} = 99, inside the 100 to 200 range they measured. In Elmer, a symmetric stack (25 µm polyimide above and below the films) places the channel at the neutral plane with a residual strain per unit curvature of 2.2×10^{-8} m.

Table 2 Model parameters with sources. 'Assumed' marks typical values or design choices without a device-specific measurement; the influence of the uncertain electrochemical parameters is quantified in Appendix D.

Parameter	Symbol	Value	Source
Polyimide substrate modulus / thickness	E_s, t_s	2.5 GPa / 25 µm (baseline)	modulus assumed (typical); thickness [21]
PET ultrathin substrate	E_s, t_s	4.0 GPa / 2.5 µm	[15]
Au electrodes	E, t	79 GPa / 50 nm	assumed (bulk modulus, typical thickness)
MoS_2 channel	E, t	270 GPa / 0.65 nm	[27]
Al_2O_3 passivation	E, t	180 GPa / 5 nm	thickness [4, 5]; modulus assumed
PMMA encapsulation	E, t	3.0 GPa / 1 µm	[22]
Poisson ratios (PI, Au, MoS_2, Al_2O_3, PET, PMMA, PDMS, island)	v	0.34, 0.44, 0.27, 0.24, 0.38, 0.35, 0.49, 0.22	assumed (typical values)
Rigid island / PDMS carrier	E, size	70 GPa, 3 mm × 20 µm / 2 MPa, 100 µm (swept 50 to 500 µm)	island [14]; carrier assumed, swept
vdW strain transfer (bare / Al_2O_3 / polymer)	η	0.5 / 0.8 / 1.0	trend [22]; values assumed, swept 0.5 to 1.0
Channel gauge factor range	GF_{min}, GF_{max}	15 to 200	[8]
Schottky barrier strain coefficient	β	−55 meV per % strain	[10]
Contact fraction of resistance	r_c	0.3 (swept 0 to 0.8)	[4, 10]

Parameter	Symbol	Value	Source
Sensitivity cross-talk	κ_x	85 per unit strain (29 % per 0.34 %)	[11]
Aptamer dissociation constant	K_D	50 nM (18.1 ng/mL)	[1, 23]
Dissociation rate	k_{off}	2×10^{-3} s^{-1}	[12] (response time)
Association rate	k_{on}	4.0×10^{4} M^{-1} s^{-1}	derived, k_{off}/K_D
Unscreened cortisol threshold shift	$\Delta V_{T,vac}$	100 mV (27 to 780 mV reported)	range [24]; value assumed
Charge distance / sweat ionic strength	d, I	2 nm / 50 mM	[25, 26]
Gate overdrive	V_{ov}	0.3 V (swept 0.05 to 1 V)	design choice
Wrist / elbow minimum bending radius	R_{min}	25 mm / 40 mm at 0.5 Hz	placement [19]; radii assumed, swept 20 to 40 mm
Walking curvature perturbation	$1/\Delta\kappa$, f	300 mm at 1.8 Hz	[20]
Prebent-channel strain ratio	—	1×10^{-3}	[13]
Physiological sweat cortisol range	—	8.16 to 141.7 ng/mL	[12]

Table 3 Consistency checks of the model against published quantities and FE verification.

Quantity	Model	Reference value	Ref.
Neutral plane, all v = 0 (Elmer vs beam theory)	13.4326 μm	13.4326 μm	(2)
ε_{ch}/κ at $\eta = 1$, all v = 0 (Elmer vs beam theory)	11.6105 μm	11.6177 μm (−0.06 %)	(2), (3)
Debye length at 100 mM	0.96 nm	about 1 nm	[16, 25]
Current change at 0.7 % tensile strain	100 % (GF_{ch} = 99)	nearly doubled (GF 100 to 200)	[8]
Sensitivity change over −0.17 to +0.17 % strain	28.9 %	29 %	[11]

Quantity	Model	Reference value	Ref.
Channel strain, symmetric stack (Elmer)	2.2×10^{-8} m per unit curvature	zero	[21]

3. Results

3.1 Peak Motion Artifacts of the Baseline Device

Fig. 3 shows the curvature and channel-strain waveforms of the three motions for the baseline device. Peak channel strains are small in absolute terms: 0.0370 percent for the wrist, 0.0231 percent for the elbow and 0.0031 percent for walking. Fig. 4(a) shows, however, that they fall on a steep electrical response. At V_{ov} = 0.3 V the corresponding peak current changes are 3.36, 2.10 and 0.28 percent of I_0, which are 44, 27 and 3.6 percent of the full-scale cortisol response respectively (Table 4). Since the whole physiological range occupies only 4.41 percent of I_0, the wrist artifact equals 76 percent of the physiological span, and the model predicts that a single wrist flexion moves the reading across most of that range.

Expressed as false concentration (Fig. 5(a)), the picture is worse because of the non-linear isotherm. With true cortisol at 30 ng/mL, walking alone produces a peak false reading of +5.4 ng/mL, and at 50 ng/mL of +11.5 ng/mL, comparable to the lower physiological limit of 8.16 ng/mL. Elbow flexion at 30 ng/mL yields +152 ng/mL, above the upper physiological limit, and wrist flexion saturates the reading at any operating point above about 20 ng/mL. The linearised errors, computed from the calibration slope at 30 ng/mL, are 56, 35 and 4.7 ng/mL for wrist, elbow and walking. These figures explain the qualitative observation of [12] that unprotected MoS_2 cortisol sensors give unreliable readings after bending. They also show that the problem is not confined to large joint motion: the small curvature changes of ordinary walking are already comparable to the lower end of the physiological range.

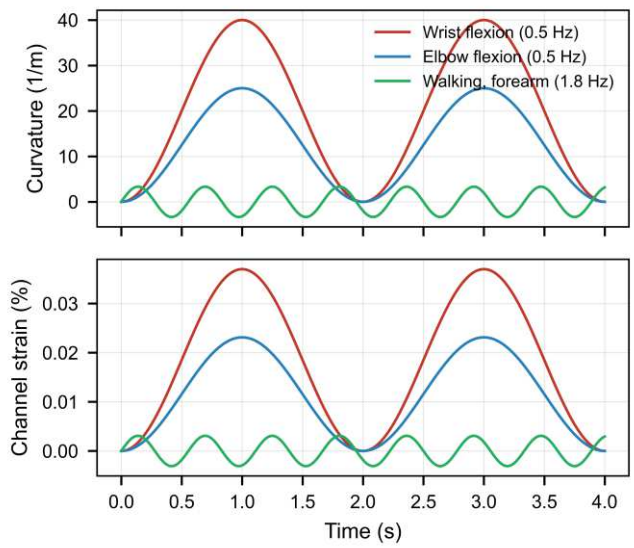


Fig. 3 *Stage 1 and 2 outputs for the baseline device: (top) curvature waveforms of wrist flexion, elbow flexion and walking; (bottom) resulting MoS_2 channel strain from the Elmer model.*

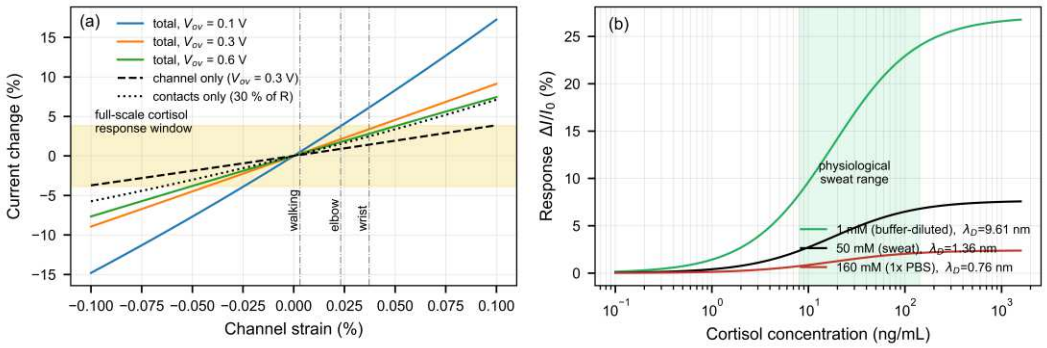


Fig. 4 *Stage 3 and 4 outputs. (a) Current change versus channel strain from (5) at three gate overdrives, with the channel-only and contact-only contributions at 0.3 V; the shaded band is the full-scale cortisol response window and the vertical lines mark the peak strains of the three motions. (b) Calibration curve from (9) at three ionic strengths, showing the compression of the cortisol signal by Debye screening in sweat and PBS.*

Table 4 Peak channel strain, current artifact and false cortisol reading for the baseline device (V_{ov} = 0.3 V, r_c = 0.3, Elmer strain).

Motion	Peak strain (%)	Current artifact (% of I_0)	Artifact (% of full scale)	C_{false} at 30 ng/mL	C_{false} at 50 ng/mL
Wrist flexion, R = 25 mm	0.0370	3.36	43.8	saturates	saturates
Sustained	0.0308	2.80	36.5	saturates	saturates

Motion	Peak strain (%)	Current artifact (% of I_0)	Artifact (% of full scale)	C_{false} at 30 ng/mL	C_{false} at 50 ng/mL
wrist hold, R = 30 mm					
Elbow flexion, R = 40 mm	0.0231	2.10	27.4	+152 ng/mL	saturates
Walking, 1/Δκ = 300 mm	0.0031	0.28	3.64	+5.4 ng/mL	+11.5 ng/mL

3.2 Contribution of the Schottky Contacts

The dashed and dotted curves of Fig. 4(a) separate the channel and contact contributions. At V_{ov} = 0.3 V the two contacts, carrying 30 percent of the resistance, contribute 64 of the total small-signal gauge factor of 90, roughly twice the channel contribution. Fig. 5(b) sweeps r_c from 0 (ideal ohmic contacts) to 0.8 (contact-dominated): the wrist artifact rises from 18 to 88 percent of full scale. This bears directly on device concepts whose signal originates at asymmetric Schottky contacts, such as the two-terminal MoS_2 diode cytokine sensor of [4]. In a flexible version, the very interface that produces the sensing signal would produce the largest motion artifact, and contact engineering (ohmic or phase-engineered contacts, or contacts placed on rigid regions) becomes a motion-artifact mitigation strategy in its own right. This also agrees with the observation that the MoS_2/Au interface is the mechanically weakest point of stretchable MoS_2 transistors [6].

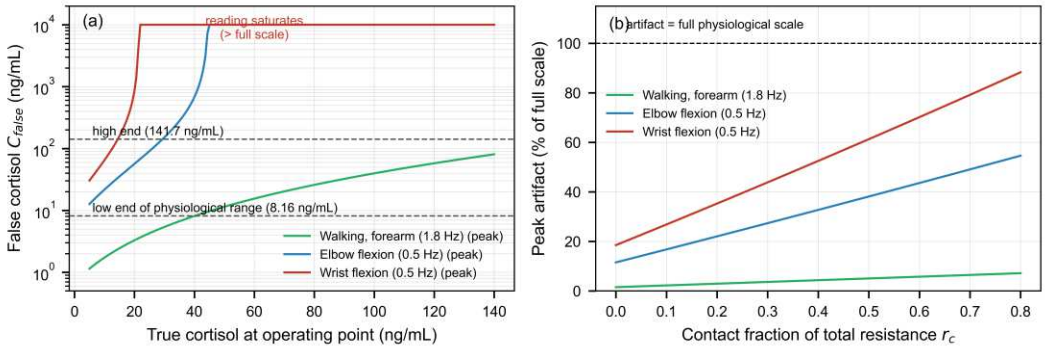


Fig. 5 *Stage 5 output. (a) Strain-equivalent false cortisol concentration at the peak of each motion versus the true concentration at the operating point; readings above full scale are shown at the top of the axis. (b) Peak artifact as a fraction of the full-scale response versus the contact share of device resistance.*

3.3 Dynamic Scenario: Filtering Versus Twin-Sensor Subtraction

Fig. 6 shows the 1800 s scenario for the baseline device and Table 5 summarises the errors by motion block. The raw reading tracks the ideal curve at rest, oscillates by tens of ng/mL

during walking (RMS 13.4, maximum 35.6 ng/mL) and saturates during wrist and elbow flexion. Low-pass filtering removes the 1.8 Hz walking oscillation but fails during unipolar flexion: the reading remains saturated, and the filter's memory smears the offset into the adjacent walking and rest blocks, raising the walking-block error to a maximum of 293 ng/mL and producing an error of up to 106 ng/mL for tens of seconds after motion stops. Because the zero-phase filter is non-causal, it also spreads each motion block backwards in time: most of the filtered error in the walking block comes from the wrist block that follows, not from walking. With matched devices, twin-sensor subtraction followed by filtering removes the additive artifact but leaves the cross-talk floor, which at the 100 ng/mL true concentration of the motion blocks amounts to 15, 20 and 13 ng/mL maximum during wrist flexion, the hold and elbow flexion (Table 5). The zero-phase filter adds no delay at the cortisol step; it spreads the step symmetrically, with the 10 to 90 percent transition between −22 and +22 s, which is short compared with the 77 s binding time constant. The causal form of the filter instead delays the step by 23 s and does not spread motion backwards; its motion-only errors are of the same size (Appendix C).

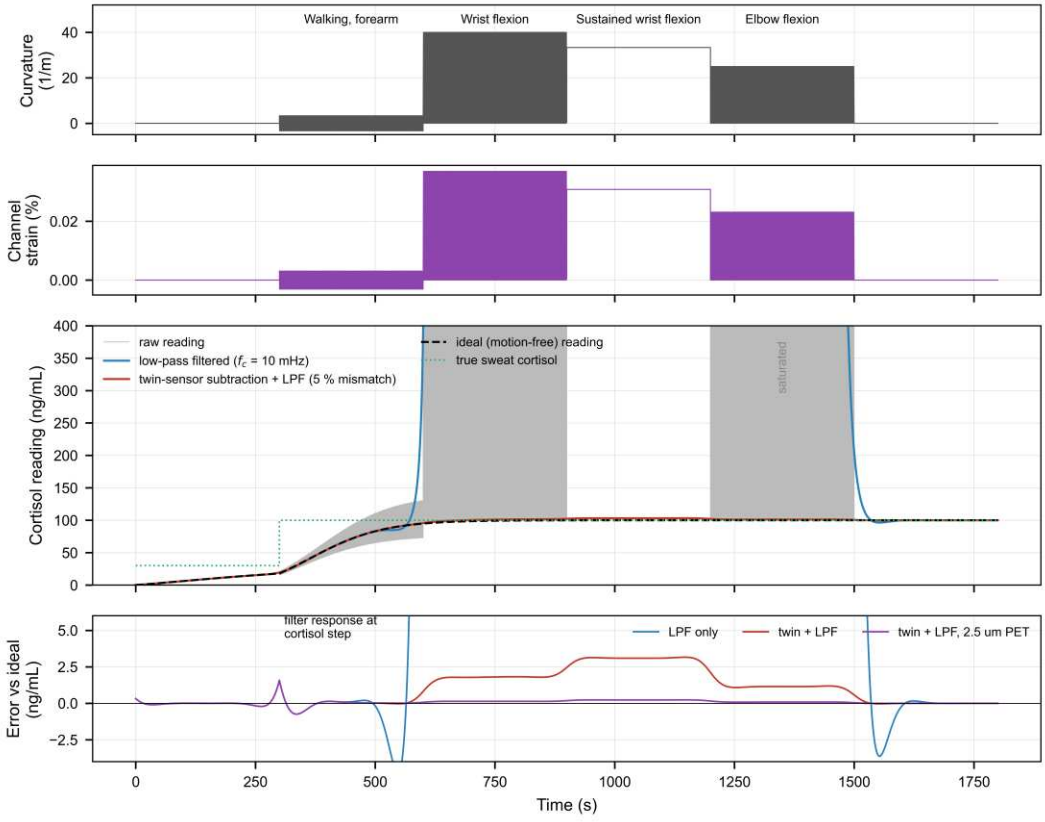


Fig. 6 *Stage 6 time-domain scenario for the baseline device. From top: scheduled patch curvature; channel strain; cortisol reading from the raw output, after low-pass filtering, and after twin-sensor subtraction with δ = +5 percent mismatch (the favourable sign; Table C1) followed by filtering, compared with the ideal motion-free reading and the true sweat concentration; bottom: error relative to the ideal reading, including the combined ultrathin-substrate and twin-sensor design.*

Table 5 Errors relative to the ideal motion-free reading in the dynamic scenario (RMS / maximum, ng/mL; zero-phase LPF, f_c = 10 mHz). Twin rows use matched devices (δ = 0); δ = ±5 percent is in Table C1. Island rows use end-moment loading. Walking and rest blocks contain the filter's spreading of the cortisol step and of adjacent motion blocks. sat. = reading saturated.

Design and processing	Walking	Wrist flexion	Sustained hold	Elbow flexion	Rest after motion
Baseline, raw	13.4 / 35.6	sat.	sat.	sat.	0 / 0
Baseline, LPF	32.3 / 293	sat.	sat.	sat.	14.6 / 106
Baseline, twin + LPF	0.85 / 4.85	11.0 / 15.4	19.6 / 20.5	6.97 / 13.0	0.55 / 3.29
12.5 µm PI, raw	5.97 / 14.2	sat.	sat.	349 / 870	0 / 0
12.5 µm PI, LPF	8.42 / 57.1	333 / 1806	sat.	112 / 492	5.20 / 33.3
12.5 µm PI, twin + LPF	0.47 / 2.21	4.87 / 6.71	8.37 / 8.72	3.14 / 5.73	0.25 / 1.51
2.5 µm PET, raw	0.95 / 2.06	19.7 / 34.4	27.4 / 27.4	11.6 / 19.4	0 / 0
2.5 µm PET, LPF	1.10 / 6.44	14.7 / 20.9	26.8 / 28.1	9.25 / 17.5	0.72 / 4.32
2.5 µm PET, twin + LPF	0.31 / 1.57	0.76 / 1.03	1.27 / 1.32	0.49 / 0.88	0.04 / 0.24
Rigid island (FE, end moment), raw	2.90 / 6.54	125 / 262	160 / 160	49.7 / 89.6	0 / 0
Rigid island (FE, end moment), LPF	3.52 / 22.3	61.3 / 100	155 / 168	34.2 / 77.2	2.32 / 14.3
Rigid island (FE, end moment), twin + LPF	0.35 / 1.57	2.34 / 3.20	3.96 / 4.12	1.52 / 2.74	0.12 / 0.74

3.4 Why Filtering Fails and What Limits Twin Subtraction

Fig. 7(a) generalises the filtering result. For a bipolar oscillation about the calibrated curvature, the filtered residual falls from its unfiltered RMS value at frequencies below f_c to below 0.1 percent of full scale in the body-motion band, so timescale filtering is effective for walking and for any symmetric vibration. For unipolar flexion the residual is independent of frequency and equals half the peak artifact, 22 percent of full scale for the wrist, because a flat-to-bent-to-flat cycle has a non-zero time average that no low-pass filter can distinguish from a slow change in cortisol. Sustained flexion is the limiting case at zero frequency. Since most joint motions are unipolar (a joint flexes from a rest posture and returns), filtering alone is not a viable compensation strategy for a wrist- or elbow-mounted sensor.

Dividing the residuals of (12) by the full-scale response $\Delta V_T/V_{ov}$ gives, as a fraction of full scale, $\theta\kappa_x\varepsilon_{ch} - \delta(\Delta I/I_0)/(\Delta V_T/V_{ov})$. Fig. 7(b) plots its magnitude at the wrist peak and 50 ng/mL for a reference channel less sensitive than the sensing channel ($\delta < 0$), where the terms add: 0.44 percent of full scale per percent of mismatch on top of a cross-talk floor of 2.3 percent. For $\delta > 0$ the terms partly cancel, but only at one strain and one concentration, so the cancellation cannot be relied on. The floor itself is not a constant: it is proportional to the aptamer occupancy θ and therefore to the operating point. Fig. 7(c) shows it across concentration: at the wrist it rises from 1.0 percent of full scale at 8.16 ng/mL to 2.8 percent at 141.7 ng/mL, with an upper bound of 3.1 percent as $\theta \to 1$. In concentration units it grows faster still at high concentration, where the isotherm flattens. The floor exists for any reference-channel scheme in which the reference carries no biomarker signal for strain to modulate; within this model it can only be lowered by reducing the strain or the cross-talk coefficient, which motivates combining structural and signal-level strategies.

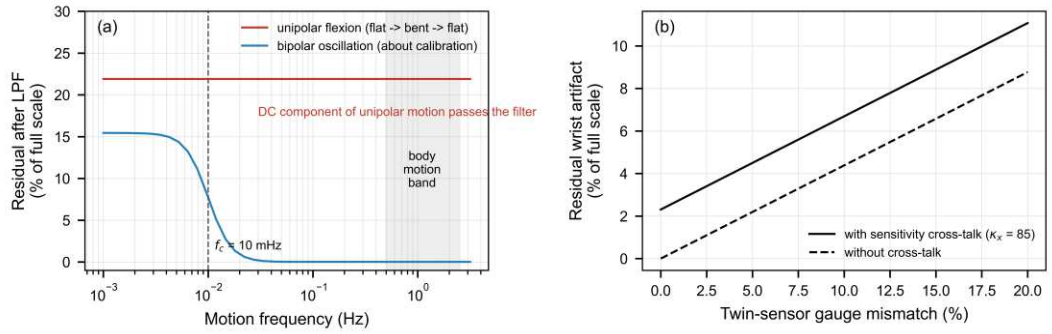


Fig. 7 *(a) Residual artifact after 10 mHz low-pass filtering versus motion frequency for unipolar flexion and bipolar oscillation of the baseline device at wrist curvature. (b) Residual wrist artifact at 50 ng/mL after twin-sensor subtraction versus the magnitude of the gauge mismatch, for a reference channel less sensitive than the sensing channel ($\delta < 0$, the unfavourable sign), with and without the strain-sensitivity cross-talk term. (c) Cross-talk floor of matched twin channels ($\delta = 0$) versus true cortisol concentration at the peak of each motion; the shaded band is the physiological range.*

3.5 Comparison of Mitigation Strategies

Fig. 8(a) ranks seven structural designs by peak artifact under the three motions, all at V_{ov} = 0.3 V and r_c = 0.3, and Table 6 gives the values from the Elmer strain. Adding a 1 µm PMMA encapsulation to the baseline makes the artifact worse, from 44 to 52 percent of full scale at the wrist, because the improved adhesion raises the strain transfer efficiency and the cap moves the neutral plane only marginally. This is the quantitative form of the trade-off identified optically in [22], and it implies that encapsulation chosen for chemical protection must be paired with a strain-reducing geometry. Halving the substrate thickness halves the artifact, and the 2.5 µm PET film used for deformable graphene aptamer sensors [15] reduces the wrist artifact to 3.3 percent of full scale, a factor of 13. The buried neutral-plane channel with an extended gate reaches 4.6 percent, limited by the 0.98 µm offset of the channel from the neutral plane; its practical value depends on the extended gate not introducing its own strain response. The rigid island reaches 10.0 percent under end-moment loading, a reduction of only 4.4 times, and increases the strain when the skin imposes the curvature (Section 3.6). The prebent channel reaches 0.044 percent, the only structural strategy that alone brings every motion below 0.1 percent of full scale, at the cost of the complex sacrificial-layer fabrication described in [13].

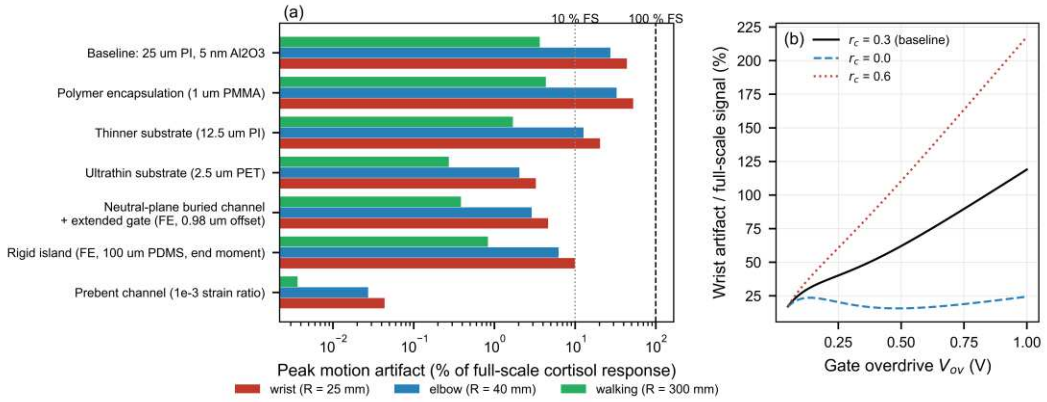


Fig. 8 *(a) Peak motion artifact as a fraction of the full-scale cortisol response for seven structural designs under wrist, elbow and walking motion; the rigid island is shown under end-moment loading. (b) Ratio of wrist artifact to full-scale signal versus gate overdrive for three contact fractions.*

Table 6 Peak artifact as a percentage of the full-scale cortisol response for the structural strategies (V_{ov} = 0.3 V, r_c = 0.3, Elmer strain).

Design	Wrist strain (%)	Wrist	Elbow	Walking	Reduction
Baseline (25 µm PI, 5 nm Al_2O_3)	0.0370	43.84	27.37	3.642	1.0×
Polymer	0.0442	52.43	32.72	4.353	0.84×

Design	Wrist strain (%)	Wrist	Elbow	Walking	Reduction
encapsulation (1 μm PMMA)					
Thinner substrate (12.5 μm PI)	0.0172	20.39	12.73	1.696	2.2×
Ultrathin substrate (2.5 μm PET)	0.0028	3.27	2.04	0.272	13.4×
Neutral-plane buried channel + extended gate	0.0039	4.64	2.90	0.386	9.5×
Rigid island (FE, 100 μm PDMS, end moment)	0.0084	9.98	6.24	0.831	4.4×
Prebent channel (1×10^{-3} strain ratio)	0.00004	0.044	0.027	0.004	1003×

Gate bias is a weaker lever than geometry. Fig. 8(b) plots the ratio of wrist artifact to full-scale signal against V_{ov}. Although GF_{ch} falls steeply with overdrive, the biomarker signal in (9) falls as $1/V_{ov}$ and the contact term in (5) is independent of gate, so the ratio rises monotonically with V_{ov} for any r_c above about 0.1: from 26 percent at 0.1 V to 44 percent at 0.3 V for the baseline. Operating close to threshold therefore helps, by a factor of about 1.7 between 0.3 and 0.1 V, but the linear-regime model does not extend into subthreshold operation, where noise and hysteresis rise, and the gain is small compared with the 13-fold to 1000-fold reductions available structurally. Only for near-ohmic contacts ($r_c = 0$) does a shallow optimum appear near 0.5 V.

The lower rows of Table 5 show the combined strategies in the dynamic scenario. The ultrathin substrate alone still produces raw errors of 34 ng/mL at the wrist and 27 ng/mL during the sustained hold, which filtering does not remove; with matched twin subtraction the maximum errors fall to 1.0, 1.3 and 0.9 ng/mL during wrist flexion, the hold and elbow flexion, compared with 6.7, 8.7 and 5.7 ng/mL for the 12.5 μm substrate and 15, 20 and 13 ng/mL for the baseline. The residual is the cross-talk floor scaled by the strain, confirming that the two classes of strategy are complementary: structure reduces the strain, and the reference channel removes the additive part of what remains. A 5 percent mismatch of

unfavourable sign roughly doubles these residuals, to 1.9, 2.4 and 1.6 ng/mL for the ultrathin substrate, whereas the favourable sign happens to reduce them to 0.2 ng/mL (Table C1).

3.6 Rigid Island Under Bending: Finite-Element Result

Isolation by a stiff island is usually quantified in stretching, where [14] reports a sensing-region strain of 4.2 percent of the stretched-region strain. Under bending the FE model gives a very different result: under end-moment loading with a 100 μm PDMS carrier, the channel above the island carries 22.8 percent of the baseline channel strain, not 4.2 percent. Two effects compete. First, the island does reduce the local curvature, to 7.75 percent of the strip average, consistent with the ratio of bending stiffnesses. Second, the island pulls the local neutral plane down into itself, about 9 μm below its top surface. The channel on top of the 25 μm polyimide film therefore sits 34.0 μm from zero strain, against 11.56 μm in the baseline: a lever arm 2.94 times longer, which undoes much of the curvature reduction.

The carrier thickness was not specified by the source design, so it was swept under the same end-moment loading (Table 7, Fig. 9). The channel strain never approaches 4.2 percent and rises with carrier thickness: a thicker PDMS stiffens the unprotected part of the strip, so a larger share of the overall bend is taken over the island. At 500 μm the island is worse than no island. The neutral-plane position under the channel is set by the island and the polyimide alone, so the 34 μm lever arm is independent of the carrier.

Table 7 Rigid-island sensitivity to the PDMS carrier thickness (Elmer, wrist bending, moment loading).

PDMS thickness (μm)	Elements	Channel strain / baseline	Island curvature / strip mean	Channel distance from neutral plane (μm)
50	7,470	18.4 %	6.26 %	34.02
100	9,960	22.8 %	7.75 %	34.03
200	15,355	47.1 %	16.0 %	34.05
500	30,710	108.5 %	36.6 %	34.24

The moment-loaded results are the favourable case for the island. To test this, the strip was solved again with the wrist curvature imposed on the PDMS underside, as by skin that dictates the patch shape (Appendix E, Table E3). The local curvature over the island then equals the imposed curvature to within 1 percent, so the island no longer reduces it, and the channel carries 292 percent of the baseline strain when the underside can slide and 329 percent when it is bonded, close to the lever-arm ratio of 294 percent. On the same mesh with the island replaced by PDMS, the channel carries 111 and 681 percent: the island lowers the strain only relative to a thick carrier bonded to skin that cannot stretch, and even then leaves 3.3 times the baseline strain. A stiff island under the channel is

therefore not a strain-isolation strategy in bending under either loading assumption, unless the channel is also kept near its own neutral plane, for example by a matching top encapsulation over the island.

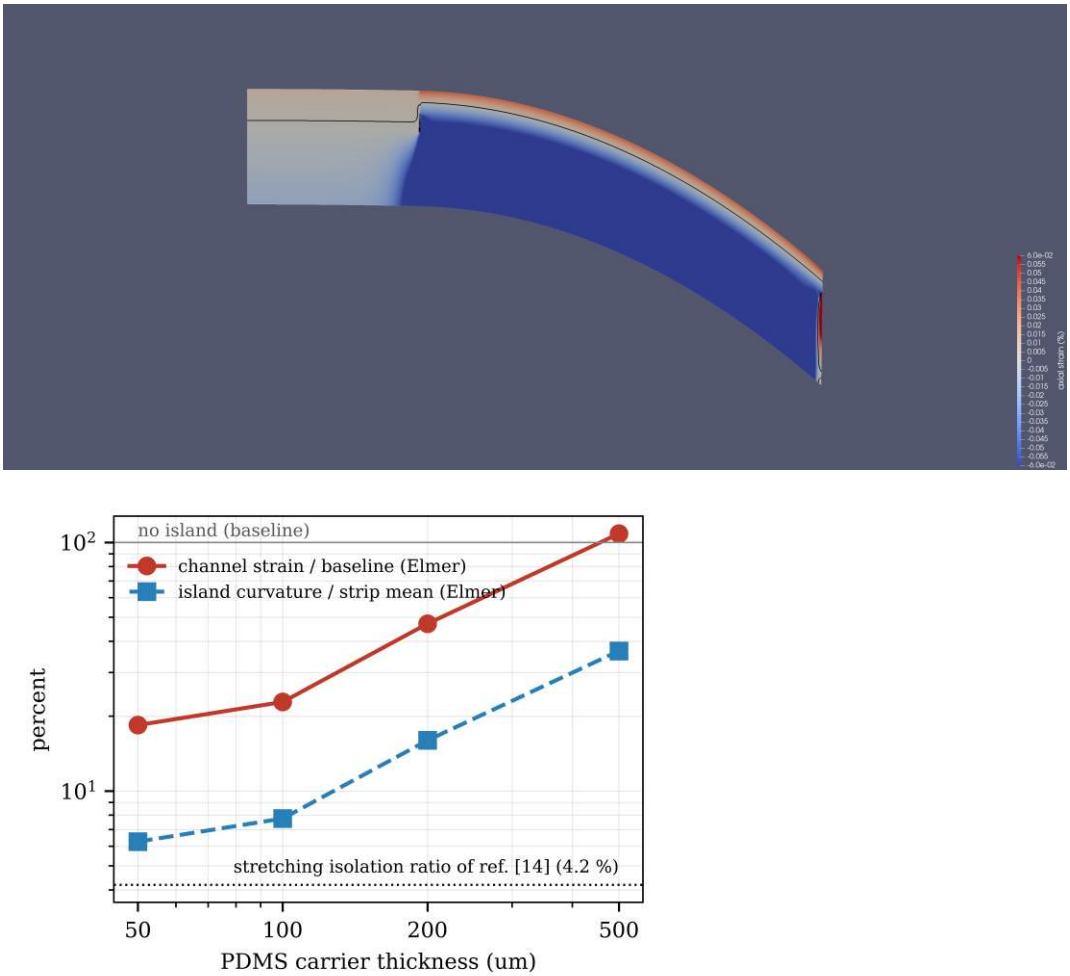


Fig. 9 *(a) Elmer strain field of the rigid-island patch in wrist bending under end-moment loading (thickness exaggerated ×8). (b) Channel strain relative to baseline versus PDMS carrier thickness under end-moment loading, with the 4.2 percent stretching ratio of [14] for comparison.*

4. Discussion

4.1 Design Guidelines

Table 8 Design guidelines by body location, assessed against a target of 1 ng/mL maximum motion-induced error. Expected residuals are maximum errors at 100 ng/mL true cortisol during the motion blocks: matched devices (δ = 0) and, in parentheses, δ = −5 percent (Table 5, Table C1); forearm values are motion-only errors of the walking-only scenario (Appendix C); prebent values scale the baseline by the strain ratio.

Location and dominant motion	Filtering alone?	Best structure studied	Twin channel	Expected residual (max)	Meets 1 ng/mL?
Forearm; walking, bipolar, 1.8 Hz	Yes (f_c about 10 mHz)	none beyond the 25 µm baseline	Optional	below 0.32 ng/mL	Yes
Dorsal wrist; flexion, unipolar, 0.5 Hz, and holds	No (22 % FS offset)	2.5 µm PET	Mandatory, closely matched	1.0 to 1.3 ng/mL (1.9 to 2.4)	No: approaches it with matched devices
Elbow; flexion, unipolar, 0.5 Hz	No	2.5 µm PET	Mandatory, closely matched	0.9 ng/mL (1.6)	Only with matched devices
Any location, no twin channel	Not required	Prebent channel (1×10^{-3} ratio)	No	below 0.05 ng/mL (scaled)	Yes (estimated by scaling)

Table 8 translates the results into guidelines by body location, taking a target of 1 ng/mL maximum motion-induced error, about one eighth of the lowest physiological concentration; every entry is traceable to Table 5, Table C1 or the walking-only scenario of Appendix C. On the forearm, where walking is the dominant motion and the curvature change is bipolar, low-pass filtering alone keeps the motion-only error below 0.32 ng/mL even for the baseline 25 µm substrate (walking-only scenario, both filter forms), so a twin channel is optional. On the dorsal wrist or the elbow, where flexion is unipolar and reaches curvatures of 25 to 40 per metre, filtering must not be relied upon. A twin reference channel is mandatory there, and it must be combined with a strain-reducing structure, because the cross-talk floor exceeds the target several-fold for every uniform substrate studied except the thinnest, and is close to it even there. The ultrathin substrate is the best of the uniform structures studied, but for K_D = 50 nM it does not consistently meet the target: with matched devices the maximum error at 100 ng/mL true cortisol is 1.03 ng/mL during wrist flexion and 1.32 ng/mL during the sustained hold, and only elbow flexion (0.88 ng/mL) stays below 1 ng/mL; with a 5 percent mismatch of unfavourable sign no flexion block meets it. With a weaker-binding aptamer (K_D = 500 nM) the matched-twin error would fall below the target (Appendix D). The joint uncertainty analysis shows that this nominal performance is not guaranteed: only 51 percent of the sampled parameter sets meet the target with the 2.5 µm PET substrate and 4 percent with the baseline (Table D3), so aptamer affinity, strain-sensitivity cross-talk and channel matching must be characterised experimentally. Of the designs studied, only low-pass filtering on the forearm and the prebent channel meet the target; the last column of Table 8 states this for each location. A

rigid island is not recommended for bending-dominated locations (Section 3.6). Prebent channels meet the target without a twin channel, by scaling, but at high fabrication cost.

In every location, contact engineering that reduces r_c is worth roughly a factor of two, polymer encapsulation should be applied only together with a strain-reducing geometry, and the gate should be biased as close to threshold as noise permits. Where a twin channel is used, the two devices should be fabricated side by side from the same film and matched as closely as possible, since the sign of the mismatch is not controlled and each percent of mismatch of the unfavourable sign adds 0.44 percent of full scale to the wrist residual.

4.2 Strain Isolation in Bending Versus Stretching

The rigid-island result has a general lesson for wearable sensor design. A strain-isolation ratio measured or computed in stretching describes how much in-plane strain the island lets through. In bending, the strain at a point is the curvature times the distance from the local neutral plane, and a stiff island changes both. It lowers the curvature above it, but it also pulls the neutral plane down into itself, so a channel placed on top of the island sits farther from zero strain than on a uniform film. In the design studied here the second effect cancels most of the first: under end-moment loading the island reduces the channel strain only 4.4-fold, not the 24-fold implied by the stretching ratio, and it is counter-productive on a thick carrier; under skin-imposed curvature it increases the strain about threefold. A stretching ratio should therefore not be applied to bending motions. To protect a channel in bending, a design must keep it near its own neutral plane, for example by an encapsulation over the island that matches the island's stiffness below it, or by the buried-channel geometry of Section 3.5.

4.3 Limitations

The model is deliberately compact, and several simplifications bound its accuracy. The mechanics are solved by two-dimensional plane-strain finite elements, which resolve the Poisson mismatch between layers and the non-uniform bending of the rigid-island patch. They do not resolve three-dimensional effects at electrode edges, finite flake length, or slip between skin and patch. The van der Waals strain transfer is applied as a literature factor η rather than modelled as a compliant interface. Poisson ratios other than that of polyimide are literature values, and the rigid-island carrier thickness and loading were not specified by the source design, so they were swept and bounded. The prebent channel is represented by its published strain ratio because an out-of-plane prebuckled structure cannot be represented in two dimensions.

The strain coefficients come from monolayer and bilayer exfoliated MoS_2 on rigid or flexible substrates measured in air. In a liquid-gated device the double-layer capacitance may alter the gate dependence of the gauge factor, and few-layer or solution-processed films [6, 12] will have different coefficients. The FET is treated in its linear regime with a single threshold shift for binding; subthreshold operation and channel-length-dependent contact effects are not modelled. The cortisol signal is bounded by a conservative choice within

the wide 27 to 780 mV range predicted in [24]; a larger true signal would proportionally reduce every artifact percentage reported here, while a smaller one would increase them. Within the bounds of Appendix D, the absolute errors scale strongly with this threshold shift, ionic strength, charge distance and aptamer affinity, whereas the qualitative conclusions (the filtering offset equal to half the peak artifact, the occupancy-proportional cross-talk floor and the dominance of the contacts for $r_c \geq 0.3$) hold throughout. Motion inputs are idealised waveforms with curvature radii taken from anatomy rather than from measured patch deformation, and the effect of strain on the aptamer binding energy itself is not treated. The main filtering results are retrospective (zero-phase); the causal filter gives errors of the same size (Appendix C), but a deployed device would also face sensor drift and noise, which are not modelled.

Finally, the model is not validated against a fabricated device. The FE mechanics are verified against beam theory and converged, and the consistency checks of Table 3 show that the electrical chain is anchored to independent published measurements. Its predictions are stated so that they can be tested experimentally with a strain rig and a two-channel readout.

5. Conclusion

A six-stage dynamic multiphysics model, with finite-element mechanics solved in the open-source Elmer FEM, links representative body motion to a strain-equivalent false cortisol reading in a flexible liquid-gated MoS_2 FET sensor operating in sweat. For a conventional 25 µm polyimide patch the model predicts that wrist flexion produces a current artifact equal to 44 percent of the full-scale cortisol response and saturates the reading, elbow flexion produces a false reading above the physiological range, and ordinary walking produces 5 to 11 ng/mL of false cortisol, comparable to the lower end of that range. About 70 percent of the artifact originates at the Schottky contacts. These magnitudes scale with the assumed cortisol-induced threshold shift.

Timescale filtering removes bipolar motion such as walking, so on the forearm filtering alone suffices, but it is defeated by the non-zero mean of unipolar joint flexion, which leaks through as a 22 percent full-scale offset. Twin-sensor subtraction removes the additive artifact but leaves a cross-talk floor proportional to aptamer occupancy, 1.0 to 2.8 percent of full scale across the physiological range at the wrist, plus a mismatch term whose sign is not controlled. With a 2.5 µm substrate and matched twin channels the maximum error falls to 0.9 to 1.3 ng/mL during flexion at 100 ng/mL, which approaches but does not consistently meet a 1 ng/mL target at the wrist for K_D = 50 nM; meeting it requires a lower strain, a lower cross-talk coefficient or, as Appendix D shows, a weaker-binding aptamer; across the joint parameter uncertainty the target is met in only about half of the cases. A rigid island under the channel, effective in stretching, retains 18 to 109 percent of the baseline channel strain under end-moment loading and about 300 percent when the skin imposes the curvature, because it moves the neutral plane away from the channel. Polymer encapsulation alone increases the artifact, and gate-bias selection yields at most a factor of two.

The three testable predictions of this work, the filtering offset, the occupancy-dependent cross-talk floor and the weak bending protection of a rigid island, can be checked experimentally, and the coefficients updated as measurements on liquid-gated flexible MoS_2 devices become available.

Statements and Declarations

Funding No funding was received for conducting this study.

Competing interests The authors have no relevant financial or non-financial interests to disclose.

Author contributions Ayomide Adeyemi and Victor Ogunyemi contributed equally to the conceptualization, methodology and simulations, the writing of the original draft, and the review and editing. Both authors read and approved the final manuscript.

Ethics approval Not applicable. The study is computational and involves no human participants, animals or patient data.

Data availability The datasets generated in this study (finite-element results, sensor-chain outputs and figure data) are publicly available under the CC BY 4.0 licence at https://github.com/ayowilfred95/mos2-motion-artifact and archived on Zenodo (https://doi.org/10.5281/zenodo.23911041).

Code availability The simulation code (the Python sensor-chain model, the Elmer FEM model generators, mesh and solver input files and the run scripts) is publicly available under the MIT licence at https://github.com/ayowilfred95/mos2-motion-artifact and archived on Zenodo (https://doi.org/10.5281/zenodo.23911041).

Appendix A Twin-Sensor Derivation

Both channels are normalised to their own zero-strain current I_0, so their outputs are dimensionless fractions of I_0. The sensing channel carries the aptamer and gives, from (9) and (10),

$$R_{sense} = \frac{\Delta V_T\,\theta}{V_{ov}}\,(1 + \kappa_x\,\varepsilon_{ch}) + A(\varepsilon_{ch}), \qquad A(\varepsilon_{ch}) = \left.\frac{\Delta I}{I_0}\right|_{strain} \qquad (A1)$$

The reference channel carries a non-binding aptamer, so its biomarker term is zero ($\theta = 0$) and the cross-talk factor has nothing to multiply. It has the same contact fraction and cross-talk coefficient and sees the same strain, and its strain response differs only by the gain mismatch $\delta = (G_{ref} - G_{sense})/G_{sense}$:

$$R_{ref} = (1 + \delta)\,A(\varepsilon_{ch}) \qquad (A2)$$

Subtracting (A2) from (A1) cancels $A(\varepsilon_{ch})$ and leaves (12). Relative to the motion-free reading $\Delta V_T\theta/V_{ov}$, the residual is

$$R_{twin} - \frac{\Delta V_T\,\theta}{V_{ov}} = \frac{\Delta V_T\,\theta}{V_{ov}}\,\kappa_x\,\varepsilon_{ch} - \delta\,A(\varepsilon_{ch}) \qquad (A3)$$

and, divided by the full-scale response $\Delta V_T/V_{ov}$, the cross-talk floor ($\delta = 0$) is $\theta\kappa_x\varepsilon_{ch}$ of full scale. Worked example at the wrist peak ($\varepsilon_{ch} = 3.70\times10^{-4}$) and 50 ng/mL ($\theta = 0.734$), with $\Delta V_T/V_{ov}$ = 7.656 percent and A = 3.356 percent of I_0: $R_{sense} = 5.619 \times 1.0314 + 3.356 = 9.152$ percent; for $\delta = +0.05$, R_{ref} = 3.524 percent and R_{twin} = 5.628 percent against the ideal 5.619 percent. The cross-talk term is +2.307 percent of full scale and the mismatch term −2.192 percent, leaving +0.115 percent. For $\delta = -0.05$ the terms add to 4.50 percent, and for $\delta = 0$ the floor alone remains, 2.31 percent of full scale.

Appendix B Worked False-Concentration Examples

Table B1 Current-to-occupancy-to-concentration chain at a true concentration of 30 ng/mL (V_{ov} = 0.3 V, r_c = 0.3, Elmer strain). Percentages are of I_0 unless stated.

Quantity	Walking peak	Wrist-flexion peak
Channel strain ε_{ch}	0.0031 %	0.0370 %
Occupancy $\theta = C/(C + K_D)$	0.623	0.623
Screened full-coverage shift ΔV_T	22.97 mV	22.97 mV
Full-scale response $\Delta V_T/V_{ov}$	7.656 %	7.656 %
Motion-free response $\Delta V_T\theta/V_{ov}$	4.773 %	4.773 %
Cross-talk factor $1 + \kappa_x\varepsilon_{ch}$	1.0026	1.0314
Strain artifact $\Delta I/I_0$, eq. (5)	0.279 %	3.356 %
Measured response R_{meas}, eq. (10)	5.064 %	8.279 %
Apparent occupancy θ_{app}, eq. (11)	0.662	1.081
Apparent concentration C_{app}	35.4 ng/mL	saturated ($\theta_{app} \geq 1$)
False concentration C_{false}	+5.4 ng/mL	saturated
Linearised error A/(dR/dC)	4.7 ng/mL	56.0 ng/mL

The linearised error divides the strain artifact by the calibration slope $dR/dC = (\Delta V_T/V_{ov})K_D/(C_0 + K_D)^2$ at C_0; it neglects both the curvature of the isotherm and the cross-talk factor, and is reported only to show the error scale where the non-linear inversion saturates.

Appendix C Filtering Implementation and Real-Time Performance

The offline filter is SciPy sosfiltfilt with a second-order Butterworth section (f_c = 10 mHz, f_s = 20 Hz), odd-symmetric extension of 9 samples at each end of the 1800 s record. It has zero phase and spreads a step symmetrically (10 to 90 percent between −22 and +22 s), but it is non-causal. The causal form, SciPy sosfilt with the initial state set to the steady state of the first sample, is what a wearable could run in real time; it delays a step by 23 s at its 50 percent point, close to the 22.5 s low-frequency group delay of the filter. Motion-only errors

compare the processed reading with the same processing applied to the motion-free signal, and so exclude each filter's response to the cortisol step.

Table C1 Maximum error (ng/mL) of twin subtraction followed by the zero-phase LPF for δ = +5 percent / 0 / −5 percent, at 100 ng/mL true cortisol.

Design	Wrist flexion	Sustained hold	Elbow flexion
Baseline (25 µm PI)	2.46 / 15.4 / 31.5	3.16 / 20.5 / 43.5	2.11 / 13.0 / 26.1
12.5 µm PI	1.14 / 6.71 / 12.8	1.46 / 8.72 / 16.9	0.98 / 5.73 / 10.9
2.5 µm PET	0.18 / 1.03 / 1.89	0.23 / 1.32 / 2.42	0.16 / 0.88 / 1.62
Rigid island (FE, end moment)	0.56 / 3.20 / 5.96	0.71 / 4.12 / 7.72	0.48 / 2.74 / 5.09

Table C2 Maximum motion-only error (ng/mL) of twin subtraction followed by the LPF, δ = −5 percent: zero-phase (offline) / causal (real-time).

Design	Wrist flexion	Sustained hold	Elbow flexion
Baseline (25 µm PI)	31.5 / 22.1	43.5 / 43.2	26.1 / 42.3
12.5 µm PI	12.8 / 9.36	16.9 / 16.8	10.9 / 16.5
2.5 µm PET	1.89 / 1.41	2.42 / 2.41	1.62 / 2.37
Rigid island (FE, end moment)	5.96 / 4.41	7.72 / 7.69	5.09 / 7.55

The causal filter gives errors of the same size; it is lower during wrist flexion, where the zero-phase filter also spreads the hold that follows backwards, and higher during elbow flexion, whose offset it carries forward into the next block. For the low-pass filter alone, the large walking-block errors of Table 5 vanish in the motion-only comparison with the causal filter (below 0.01 ng/mL), confirming that they are spread from the following wrist block. In a separate walking-only scenario (walking throughout 1800 s, cortisol step at 900 s, δ = −5 percent), the maximum motion-only error after the LPF alone is 0.32, 0.15 and 0.02 ng/mL for the baseline, 12.5 µm and 2.5 µm substrates with the zero-phase filter, and below 0.01 ng/mL for all three with the causal filter.

Appendix D Sensitivity and Robustness

Table D1 Sensitivity of the baseline device to the wrist bending radius and the strain-transfer efficiency (the walking error does not depend on R_{min}).

R_{min} (mm)	η	Wrist artifact (% FS)	Filtering offset (% FS)	Walking C_{false} at 30 ng/mL	Floor at 50 ng/mL (% FS)
20	0.5 / 0.8 / 1.0	34.2 / 54.8 / 68.6	17.1 / 27.4 / 34.3	3.2 / 5.4 / 7.0	1.80 / 2.88 / 3.60
25	0.5 / 0.8 / 1.0	27.4 / 43.8 /	13.7 / 21.9 /	3.2 / 5.4 / 7.0	1.44 / 2.31 /

R_{min} (mm)	η	Wrist artifact (% FS)	Filtering offset (% FS)	Walking C_{false} at 30 ng/mL	Floor at 50 ng/mL (% FS)
		54.8	27.4		2.88
30	0.5 / 0.8 / 1.0	22.8 / 36.5 / 45.7	11.4 / 18.3 / 22.8	3.2 / 5.4 / 7.0	1.20 / 1.92 / 2.40
40	0.5 / 0.8 / 1.0	17.1 / 27.4 / 34.2	8.5 / 13.7 / 17.1	3.2 / 5.4 / 7.0	0.90 / 1.44 / 1.80

Table D2 Robustness of the headline results to the uncertain electrochemical parameters (one parameter varied at a time, others at their Table 2 values; baseline device, wrist R = 25 mm).

Parameter	Range	Wrist artifact (% FS)	Walking C_{false} at 30 ng/mL	Floor at 50 ng/mL (% FS)	Contact share of artifact
$\Delta V_{T,vac}$	27 to 780 mV	162 to 5.6	27.4 to 0.8 ng/mL	2.31	0.71
K_D	10 to 200 nM	43.8	18.9 to 5.7 ng/mL	2.93 to 1.28	0.71
κ_x	0 to 170	43.8	5.2 to 5.7 ng/mL	0 to 4.61	0.71
r_c	0 to 0.6	18.5 to 70.2	2.3 to 9.0 ng/mL	2.31	0 to 0.89
Ionic strength I	20 to 100 mM	25.5 to 80.6	3.1 to 10.7 ng/mL	2.31	0.71
Charge distance d	1 to 3 nm	21.0 to 91.5	2.6 to 12.5 ng/mL	2.31	0.71
GF_{max}	100 to 300	39.4 to 48.3	4.9 to 6.0 ng/mL	2.31	0.78 to 0.64
V_{ov}	0.1 to 0.6 V	26.4 to 72.6	3.1 to 9.6 ng/mL	2.31	0.40 to 0.84

The absolute size of the artifact is most sensitive to the screened cortisol signal ($\Delta V_{T,vac}$, I, d), which sets the full-scale response; with the largest reported shift of 780 mV the wrist artifact falls to 5.6 percent of full scale. The structural conclusions do not depend on these values: the filtering offset is always half the peak artifact, the floor depends only on θ, κ_x and the strain, and the contacts dominate the artifact whenever $r_c \geq 0.3$.

Boundary values of K_D. The two values reported for the aptamer of [1], about 30 pM on the FET and 500 nM in solution, bracket the 10 to 200 nM range of Table D2. Neither changes the artifact as a fraction of full scale (43.8 percent at the wrist), the filtering offset (21.9 percent) or the contact share (0.71), because these do not depend on the isotherm. With

30 pM the aptamer is saturated ($\theta > 0.998$) over the whole physiological range, so the sensor has no usable calibration slope and any motion that raises the current drives the reading to saturation, so this bound is not a usable design point. With 500 nM the occupancy is lower, so the cross-talk floor at 50 ng/mL falls to 0.68 percent of full scale, while the shallower isotherm raises the walking false reading at 30 ng/mL to 9.5 ng/mL. The peak wrist error of matched twin channels on the 2.5 µm PET substrate at 100 ng/mL, before filtering, falls from 1.55 ng/mL at 50 nM to 0.37 ng/mL at 500 nM, which would meet the 1 ng/mL target. Whether that target is met therefore depends on the aptamer affinity, whereas the qualitative conclusions do not.

Joint uncertainty. Table D2 varies one parameter at a time. To vary them together, 10 000 parameter sets were drawn at random: $\Delta V_{T,vac}$ and K_D log-uniformly over 27 to 780 mV and 10 to 500 nM, and uniformly κ_x (0 to 170), r_c (0 to 0.6), the barrier coefficient β (−27.5 to −82.5 meV per percent strain, ±50 percent), ionic strength (20 to 100 mM), charge distance (1 to 3 nm), GF_{max} (100 to 300), wrist radius (20 to 40 mm), η (0.5 to 1.0) and twin mismatch δ (−5 to +5 percent). The inputs are sampled independently, because no correlation between them has been measured, with the NumPy PCG64 generator (default_rng, seed 1). $\Delta V_{T,vac}$ and K_D are sampled log-uniformly because their reported values span more than an order of magnitude, so each decade is equally likely; the other ranges span a factor of five or less, or include zero, and with no evidence favouring any value inside them they are sampled uniformly. Repeating the analysis with two other seeds changes the medians by less than 5 percent and the probabilities by less than 2 percentage points. Table D3 gives the median, the central 95 percent interval and the most influential inputs of each output, ranked by the magnitude of the Spearman rank correlation ρ. The wide intervals of the artifact follow mainly from the 29-fold range of $\Delta V_{T,vac}$, which scales the full-scale response. The wrist artifact exceeds 10 percent of full scale in 74 percent of the draws, the contacts carry more than half of it in 73 percent, and twin channels on the baseline substrate meet the 1 ng/mL target in only 4 percent. On the 2.5 µm PET substrate the twin error has a median of 0.98 ng/mL and meets the target in 51 percent of the draws, depending mainly on K_D, κ_x and δ; the verdict for this design is therefore uncertain, whereas the qualitative conclusions hold across the joint range.

Table D3 Joint uncertainty from 10 000 Monte Carlo draws (ranges in the text). Twin errors are peak wrist errors at 100 ng/mL true cortisol before filtering, including the drawn mismatch δ; ρ = magnitude of the Spearman rank correlation.

Output	Median	95 % interval	Most influential inputs (ρ)
Wrist artifact (% FS)	24.4	2.4 to 241	$\Delta V_{T,vac}$ (0.80), d (0.35), r_c (0.26)
Walking C_{false} at 30 ng/mL (ng/mL)	4.4	0.5 to 266	$\Delta V_{T,vac}$ (0.78), d (0.34), r_c (0.25)
Contact share of artifact	0.69	0.07 to 0.91	r_c (0.93), β (0.27), GF_{max} (0.18)

Output	Median	95 % interval	Most influential inputs (ρ)
Twin error, baseline (ng/mL)	13.9	0.6 to saturated	K_D (0.63), κ_x (0.41), δ (0.31)
Twin error, 2.5 µm PET (ng/mL)	0.98	0.04 to 9.9	K_D (0.63), κ_x (0.40), δ (0.29)

Appendix E Finite-Element Details

All models use ElmerSolver 26.2 (StressSolver, plane strain, linear elasticity) with eight-node quadrilateral elements and a direct solver (UMFPACK). Each model represents half of the strip, from the channel centre ($x = 0$) to the free end. Uniform stacks: $u_x = 0$ on the symmetry plane $x = 0$, which suppresses horizontal translation and rotation; $u_y = 0$ at the bottom node of that plane, which suppresses vertical translation; a linear normal traction with zero net force on the end face, which applies a pure moment; all other boundaries traction-free; all interfaces perfectly bonded. The van der Waals transfer factor η is applied afterwards. Rigid-island strip under end-moment loading: the same constraints, with the moment traction applied through the polyimide end face and the PDMS end face traction-free. Under skin-imposed curvature there is no end load; instead $u_y = -\kappa x^2/2$ on the PDMS underside (wrist $\kappa = 40\ m^{-1}$), with $u_x = 0$ there in the bonded case and u_x free in the sliding case, together with $u_x = 0$ at $x = 0$. These constraints suppress all rigid-body motion, and all other boundaries are traction-free. The model generators and solver input files are included in the code described under Code availability.

Table E1 Mesh convergence of the 2.5 µm PET stack (same refinement levels as Table 1).

Level	Elements	Element length (nm)	PET element rows	ε_{ch}/κ, bonded (µm)	Change vs finest
1	11,900	118	4	0.864039	+0.007 %
2	21,600	83	6	0.864043	+0.007 %
3 (used)	37,400	59	8	0.864035	+0.006 %
4	72,000	42	12	0.863982	0

Table E2 Mesh convergence of the rigid-island strip (100 µm PDMS, end-moment loading).

Mesh scale	Elements	Channel strain / baseline	Change vs finest
0.5	2,484	22.837 %	+0.025 %
1 (used)	9,960	22.833 %	+0.010 %
2	39,840	22.831 %	0

Table E3 Channel strain of the 100 µm PDMS strip under skin-imposed wrist curvature, with and without the island (island replaced by PDMS on the same mesh), relative to the baseline value $\varepsilon_{ch}/\kappa = 11.556$ µm (bonded films, before η).

Underside condition	Island	Local / imposed curvature	ε_{ch}/κ (μm)	Relative to baseline
Free to slide	yes	0.991	33.7	292 %
Free to slide	no	1.000	12.8	111 %
Bonded, cannot stretch	yes	1.001	38.0	329 %
Bonded, cannot stretch	no	1.000	78.7	681 %

References

1. Wang, B., Zhao, C., Wang, Z., Yang, K.-A., Cheng, X., Liu, W., Yu, W., Lin, S., Zhao, Y., Cheung, K.M., Lin, H., Hojaiji, H., Weiss, P.S., Stojanović, M.N., Tomiyama, A.J., Andrews, A.M., Emaminejad, S.: Wearable aptamer-field-effect transistor sensing system for noninvasive cortisol monitoring. Sci. Adv. **8**, eabk0967 (2022). https://doi.org/10.1126/sciadv.abk0967
2. Parlak, O., Keene, S.T., Marais, A., Curto, V.F., Salleo, A.: Molecularly selective nanoporous membrane-based wearable organic electrochemical device for noninvasive cortisol sensing. Sci. Adv. **4**, eaar2904 (2018). https://doi.org/10.1126/sciadv.aar2904
3. Jang, H.-J., Lee, T., Song, J., Russell, L., Li, H., Dailey, J., Searson, P.C., Katz, H.E.: Electronic cortisol detection using an antibody-embedded polymer coupled to a field-effect transistor. ACS Appl. Mater. Interfaces **10**, 16233–16237 (2018). https://doi.org/10.1021/acsami.7b18855
4. De Silva, T., Fawzy, M., Hasani, A., Ghanbari, H., Abnavi, A., Askar, A., Ling, Y., Mohammadzadeh, M.R., Kabir, F., Ahmadi, R., Rosin, M., Kavanagh, K.L., Adachi, M.M.: Ultrasensitive rapid cytokine sensors based on asymmetric geometry two-dimensional MoS_2 diodes. Nat. Commun. **13**, 7593 (2022). https://doi.org/10.1038/s41467-022-35278-2
5. Chen, Y., Pham, T., Mulchandani, A.: 2D MoS_2-based flexible optoelectronic for biosensing. Sens. Actuators B Chem. **439**, 137848 (2025). https://doi.org/10.1016/j.snb.2025.137848
6. Kim, K., Kuzumoto, Y., Jung, C., Heo, S., Zou, T., Byeon, G., Kang, H., et al.: Intrinsically stretchable 2D MoS_2 transistors. Nat. Commun. **17**, 1796 (2026). https://doi.org/10.1038/s41467-026-68504-2
7. Nguyen, T.T.-H., Nguyen, C.M., Huynh, M.A., Vu, H.H., Nguyen, T.-K., Nguyen, N.-T.: Field effect transistor based wearable biosensors for healthcare monitoring. J. Nanobiotechnol. **21**, 411 (2023). https://doi.org/10.1186/s12951-023-02153-1
8. Datye, I.M., Daus, A., Grady, R.W., Brenner, K., Vaziri, S., Pop, E.: Strain-enhanced mobility of monolayer MoS_2. Nano Lett. **22**, 8052–8059 (2022). https://doi.org/10.1021/acs.nanolett.2c01707

9. Varghese, A., Pandey, A.H., Sharma, P., Yin, Y., Medhekar, N.V., Lodha, S.: Electrically controlled high sensitivity strain modulation in MoS_2 field-effect transistors via a piezoelectric thin film on silicon substrates. Nano Lett. **24**, 8472–8480 (2024). https://doi.org/10.1021/acs.nanolett.4c00357
10. John, A.P., Thenapparambil, A., Thalakulam, M.: Strain-engineering the Schottky barrier and electrical transport on MoS_2. Nanotechnology **31**, 275703 (2020). https://doi.org/10.1088/1361-6528/ab83b7
11. Li, P., Zhang, D., Wu, Z.: Flexible MoS_2 sensor arrays for high performance label-free ion sensing. Sens. Actuators A Phys. **286**, 51–58 (2019). https://doi.org/10.1016/j.sna.2018.12.026
12. Aleksandrova, M., Tomov, R., Tzaneva, B., Iliev, I.: Effect of microresistor topology on the sensing characteristics of MoS_2-based chemoresistive cortisol sensors. Sensors **26**, 551 (2026). https://doi.org/10.3390/s26020551
13. Ryu, B., Yang, E., Park, Y., Kurabayashi, K., Liang, X.: Fabrication of prebent MoS_2 biosensors on flexible substrates. J. Vac. Sci. Technol. B **35**, 06G805 (2017). https://doi.org/10.1116/1.4991749
14. Shen, Y., Li, Z., Xiang, Y., Feng, J., Zhang, X., Wang, T.: Decoupling stretching and sensing regions to achieve strain-insensitive iontronic pressure sensors for gesture recognition. Chem. Eng. J. **516**, 163763 (2025). https://doi.org/10.1016/j.cej.2025.163763
15. Wang, Z., Hao, Z., Yu, S., Huang, C., Pan, Y., Zhao, X.: A wearable and deformable graphene-based affinity nanosensor for monitoring of cytokines in biofluids. Nanomaterials **10**, 1503 (2020). https://doi.org/10.3390/nano10081503
16. Nakatsuka, N., Yang, K.-A., Abendroth, J.M., Cheung, K.M., Xu, X., Yang, H., Zhao, C., Zhu, B., Rim, Y.S., Yang, Y., Weiss, P.S., Stojanović, M.N., Andrews, A.M.: Aptamer–field-effect transistors overcome Debye length limitations for small-molecule sensing. Science **362**, 319–324 (2018). https://doi.org/10.1126/science.aao6750
17. Huang, H., Cai, X., Wan, S., Sun, L.: Source-level motion artifact suppression in wearable electrodes: from underlying mechanisms to advanced strategies. Mater. Today Bio **38**, 103241 (2026). https://doi.org/10.1016/j.mtbio.2026.103241
18. Rajbongsi, U.K., Gogoi, K., Goswami, R., Mondal, B.: Insights into design and operation of MoS_2–FET label-free biosensors. ECS J. Solid State Sci. Technol. **14**, 067001 (2025). https://doi.org/10.1149/2162-8777/addf7b
19. Wessendorf, A.M., Newman, D.J.: Dynamic understanding of human-skin movement and strain-field analysis. IEEE Trans. Biomed. Eng. **59**, 3432–3438 (2012). https://doi.org/10.1109/TBME.2012.2215859
20. Pachi, A., Ji, T.: Frequency and velocity of people walking. Struct. Eng. **83**(3), 36–40 (2005)
21. Rogers, J.A., Someya, T., Huang, Y.: Materials and mechanics for stretchable electronics. Science **327**, 1603–1607 (2010). https://doi.org/10.1126/science.1182383

22. Vladimirov, S.N., Çakıroğlu, O., Munuera, C., Castellanos-Gomez, A., Vasconcelos, T.L.: Enhanced strain transfer and optoelectronic performance in MoS_2 devices via Formvar encapsulation. 2D Mater. **12**, 025013 (2025). https://doi.org/10.1088/2053-1583/adabf4
23. Martin, J.A., Chávez, J.L., Chushak, Y., Chapleau, R.R., Hagen, J., Kelley-Loughnane, N.: Tunable stringency aptamer selection and gold nanoparticle assay for detection of cortisol. Anal. Bioanal. Chem. **406**, 4637–4647 (2014). https://doi.org/10.1007/s00216-014-7883-8
24. Boschetto, G., Carapezzi, S., Todri-Sanial, A.: Supported Pt nanoclusters on single-layer MoS_2 for the detection of cortisol: from atomistic scale to device modeling. ACS Appl. Electron. Mater. **5**, 2977–2987 (2023). https://doi.org/10.1021/acsaelm.2c01722
25. Stern, E., Wagner, R., Sigworth, F.J., Breaker, R., Fahmy, T.M., Reed, M.A.: Importance of the Debye screening length on nanowire field effect transistor sensors. Nano Lett. **7**, 3405–3409 (2007). https://doi.org/10.1021/nl071792z
26. Baker, L.B.: Physiology of sweat gland function: the roles of sweating and sweat composition in human health. Temperature **6**, 211–259 (2019). https://doi.org/10.1080/23328940.2019.1632145
27. Bertolazzi, S., Brivio, J., Kis, A.: Stretching and breaking of ultrathin MoS_2. ACS Nano **5**, 9703–9709 (2011). https://doi.org/10.1021/nn203879f
28. Ruokolainen, J., Malinen, M., Råback, P., Zwinger, T., Pursula, A., Byckling, M.: ElmerSolver Manual. CSC – IT Center for Science, Espoo, Finland (2026). https://www.elmerfem.org. Accessed 21 October 2026
29. Ahrens, J., Geveci, B., Law, C.: ParaView: an end-user tool for large-data visualization. In: Hansen, C.D., Johnson, C.R. (eds.) The Visualization Handbook, pp. 717–731. Elsevier, Burlington, MA (2005)